coatings

MDPI

Article

Suspended-Target Laser Deposition of Bioactive Glass on Laser-Textured Magnesium Alloy

Chenkai Zhu *, Yong Wang, Zhenzong Shao and Libin Lu *

Ningbo Institute of Technology, Beihang University, 399 Kangda Road, Ningbo 315832, China; wang04062810@gmail.com (Y.W.); shaozz@buaa.edu.cn (Z.S.)

* Correspondence: chenkaizhu@buaa.edu.cn (C.Z.); lulibin@buaa.edu.cn (L.L.)

Abstract

Rapid corrosion and poor coating adhesion continue to limit the use of magnesium alloys as temporary orthopedic implants. The two-stage laser process was developed to separate the high-temperature melting of 45S5 bioactive glass (BG) from the low-melting-point AZ31 substrate. Femtosecond-laser grids with spacings of 100, 200, and 300 μm were first produced on AZ31 to provide anchoring sites. Then, the target 45S5 BG was suspended above the substrate, locally melted with CO_2 laser, and transported onto the textured surface by gas jet. The 200 μm grid texture for Mg substrate with lowest water contact angle could give the highest tape-test adhesion rating (4B). At the selected deposition conditions of 20 W and 20 L·min^{-1}, two coating cycles produced a continuous layer approximately 50.5 μm thick. Relative to bare Mg alloy, this double-layer coating increased polarization resistance from 1.20 × 103 to 1.39 × 10^5 Ω·cm^2 and decreased corrosion current density from 8.70 × 10^{-4} to 5.33 × 10^{-6} A·cm^{-2}. It also limited alkalization and mass loss during 28 days in simulated body fluid. As such, the double-layer surface coating supported apatite formation and improved MC3T3-E1 proliferation and alkaline phosphatase activity. These findings indicated that suspended-target deposition was able to form adherent, bioactive glass coatings on magnesium while limiting direct thermal damage to the substrate.

Keywords: magnesium alloy; bioactive glass; femtosecond laser texturing; laser melt blowing; corrosion resistance; cytocompatibility

1. Introduction

Magnesium alloys are being developed as temporary fixation materials because their stiffness is closer to that of bone than that of conventional titanium, cobalt-chromium, and stainless-steel implants. They can also degrade after tissue repair, which may remove the need for a second operation. Clinical and preclinical studies now support the feasibility of magnesium-based screws and other fixation devices, although consistent control of degradation remains a prerequisite for broader use [1,2].

The biological role of magnesium is more than passive resorption. Mg^{2+} participates in bone metabolism and can affect osteoblasts, endothelial cells, sensory nerves, and immune cells. Reviews of degradable magnesium implants have linked local Mg^{2+} availability to osteogenesis, angiogenesis, and bone remodeling [3]. In animal models, magnesium released from intramedullary implants increased neuronal calcitonin gene-related peptide and improved fracture healing [4]. Controlled degradation of clinically relevant alloys has also been associated with coupled angiogenesis and osteogenesis [5]. Regarding concentration matters, a moderate Mg^{2+} microenvironment promoted bone formation in

Check for updates

Academic Editors: Anna Palau, Gaopeng Xu and Jiang Ju

Received: 22 July 2026
Revised: 6 August 2026
Accepted: 11 August 2026
Published: 12 August 2026

Copyright: © 2026 by the authors. Licensee MDPI, Basel, Switzerland. This article is an open access article distributed under the terms and conditions of the Creative Commons Attribution (CC BY) license.

a three-dimensional model, whereas excessive Mg^{2+} impaired adhesion and osteogenic differentiation [6].

This narrow biological window is difficult to maintain because magnesium corrodes rapidly in aqueous chloride-containing media. Anodic magnesium dissolution is coupled to cathodic water reduction, with Mg^{2+}, OH^-, and H_2 produced at the interface. The resulting $Mg(OH)_2$-rich film is only partly protective and is destabilized in chloride-containing solutions. Test-medium composition, buffering, renewal rate, and transport conditions can all change the apparent corrosion rate [7]. In addition, hydrogen accumulation is also important; restricted transport near the implant can alter local chloride and hydroxide concentrations and decouple measured hydrogen evolution from the actual loss of metal [8]. For the implant, uncontrolled degradation can therefore combine early loss of mechanical integrity with gas formation and local pH variation that is unfavorable for cell attachment.

Surface coatings could offer direct means of delaying electrolyte access while adding biological function. Recent assessments of coatings on degradable magnesium emphasize that protection depends on coating continuity, adhesion, and the ability to accommodate substrate degradation, not simply on initial thickness [9]. Bioactive glass is particularly attractive because it can add bone-bonding surface to metallic substrate [10]. Studies of bioactive glass coatings on magnesium have nevertheless identified recurring interfacial problems, including porosity, cracking, weak adhesion, and local corrosion beneath coating defects [11].

45S5 bioactive glass contains 45 wt% SiO_2, 24.5 wt% Na_2O, 24.5 wt% CaO, and 6 wt% P_2O_5. In aqueous media, exchange of network-modifying ions with protons is followed by silica-network hydrolysis and calcium-phosphate precipitation. The surface can then develop a hydroxycarbonate-apatite-like layer that supports bone bonding [12]. Recent studies continue to use 45S5 as a reference composition for bone regeneration, while also showing that its rapid dissolution, pH response, and tendency to crystallize during heating must be considered during processing [13].

Coating of 45S5 BG onto magnesium is therefore a coupled processing issue. Sol–gel and electrophoretic routes can operate at relatively low temperature but may produce thin or porous layers whose durability depends strongly on substrate pretreatment. Thermal spraying can deposit thicker glass coatings, whilst particle melting, crystallization, thermal-expansion mismatch, and cooling history determine adhesion and dissolution [14]. Laser texturing is a useful pretreatment because grooves or grids increase the available contact area and provide mechanical anchoring. For AZ31 Mg alloy, the depth and geometry of laser textures have been shown to affect both bond strength and corrosion behavior of a subsequent conversion coating [15]. Femtosecond-laser processing can also create hydrophilic structures that substantially improve the attachment of a deposited polymer layer to magnesium [16].

However, direct laser melting of glass on magnesium introduces a separate difficulty. The processing temperature of silicate glass is well above the melting point of Mg alloy, so laser energy density sufficient to melt the glass may also melt, vaporize, or chemically dilute the Mg substrate. A recent hierarchical glass-based coating on laser-textured Mg alloy demonstrated the value of mechanical interlocking but also documented the need to manage pores and thermal damage [17]. Laser-directed energy deposition of bioactive glass on a higher-melting titanium alloy has shown that dense glass–metal architectures can be produced, although elemental transfer and heat-affected microstructures remain concerns [18]. For magnesium, the heat source must be separated from the substrate more effectively.

In this study, combined effects of femtosecond-laser texturing and suspended-target BG deposition on AZ31 Mg alloy were investigated. Grid spacings of 100, 200, and

300 μm were first compared to determine their influence on surface wettability and coating adhesion. Using selected texture, effects of laser power, gas flow rate, and deposition cycle number were then examined to identify suitable deposition conditions. Coating phase composition, morphology, electrochemical behavior, long-term degradation, mineralization, and MC3T3-E1 response were evaluated to clarify how processing parameters affected coating integrity, corrosion protection, and biological performance.

2. Materials and Methods

2.1. Materials Preparation

Mg alloys (AZ31D) were purchased from Mingmei Technology Co., Ltd. (Hebi, China), with detail mass composition (Mg 97.121%, Al 2.117%, Zn 0.431%, Mn 0.283%, Si 0.028%, Cu 0.017%, Fe 0.002%, Ni 0.001%), and these materials were cut into standardized pellets measuring 10 × 10 × 2 mm^3 using a waterjet machine (ProtoMAX, OMAX Corporation, Kent, WA, USA). To produce an optically planar substrate surface and eliminate the native oxide layer, the specimens were sequentially ground using an automatic grinder–polisher (LMP-3S, REEDEA, Ningbo, China) with silicon carbide (SiC) waterproof abrasive papers from 400, 800, 1500, to 2000 grit. Each grade was applied for 2 min at 150 rpm under normal load of 15 N and continuous deionized-water lubrication. No additional polishing was performed after 2000-grit grinding.

The ground pellets were subsequently degreased and cleaned ultrasonically in absolute ethanol (99%, Aladdin Biochemical Technology Co., Ltd., Shanghai, China) for 15 min, followed by drying under a cool air blower. Mg-C represented untreated control surface prepared from the same AZ31D alloy batch. Mg-C specimens underwent the grinding and cleaning procedures described above but received neither femtosecond-laser texturing nor bioactive glass deposition. The bioactive glass (BG) particles with diameters in the range of 5~40 μm, based on formulation of 45S5 (45% SiO_2, 24.5% Na_2O, 24.5% CaO, 6% P_2O_5), were provided by Nanjing Fiberglass Research & Design Institute Co., Ltd. (Nanjing, China). According to SEM observation, the powder consisted mainly of irregular particles with rough surfaces (Figure S1).

2.2. Femtosecond-Laser Texturing for Mg Alloys

The ground AZ31D specimens were textured using a femtosecond fiber laser system (HR-Femto-IR-50-40B, Wuhan Huaray Precision Laser Co., Ltd., Wuhan, China) operating at a wavelength of 1035 nm, a nominal output power of 50 W, and a pulse duration of 350 fs. Parallel line-groove micro-channels were engraved on the substrate surfaces at a constant scanning speed of 200 mm/s. To systematically screen the spatial frequency effect, the scanning spaces were designed at discrete gradients of 100 μm, 200 μm, and 300 μm, and the corresponding textured substrates were denoted as Mg-D100, Mg-D200, and Mg-D300, respectively. Following laser micro-machining, all textured samples were re-washed ultrasonically in absolute ethanol (99%, Aladdin Biochemical Technology Co., Ltd., Shanghai, China) for 15 min and air-dried to remove physically adsorbed ablation splatter.

2.3. BG Coating for Textured Mg Alloy

A compacted suspended target was prepared to reduce powder drift and feedstock loss during laser processing. 45S5 BG powder was placed in a stainless-steel mold with internal cavity dimensions of 100 × 50 mm^2 and uniaxially compacted at 10 MPa for 10 min using hydraulic press, then placed in a muffle furnace (KSL-1200X, Kejing Materials Technology Co., Ltd., Hefei, China), heated from room temperature to 500 °C at a rate of 5 °C min^{-1}, held for 2 h, and then naturally cooled to room temperature. This treatment provided sufficient handling strength before laser processing.

As shown in Figure 1, the deposition of the bioactive glass coating was performed using a customized laser surface modification strategy configured to establish total spatial thermodynamic decoupling from the vulnerable magnesium matrix. The pre-cast AZ31 specimen was secured horizontally on a processing platform, while the pre-sintered 45S5 glass plate was suspended inside a customized mechanical holder at a precise spatial distance directly above the substrate. A continuous nanosecond CO_2 laser provided by Xianhui Laser Co., Ltd., Ningbo, China (λ = 10.6 μm, focal spot diameter: 100 μm) was focused perpendicularly onto the upper facet of the suspended glass target.

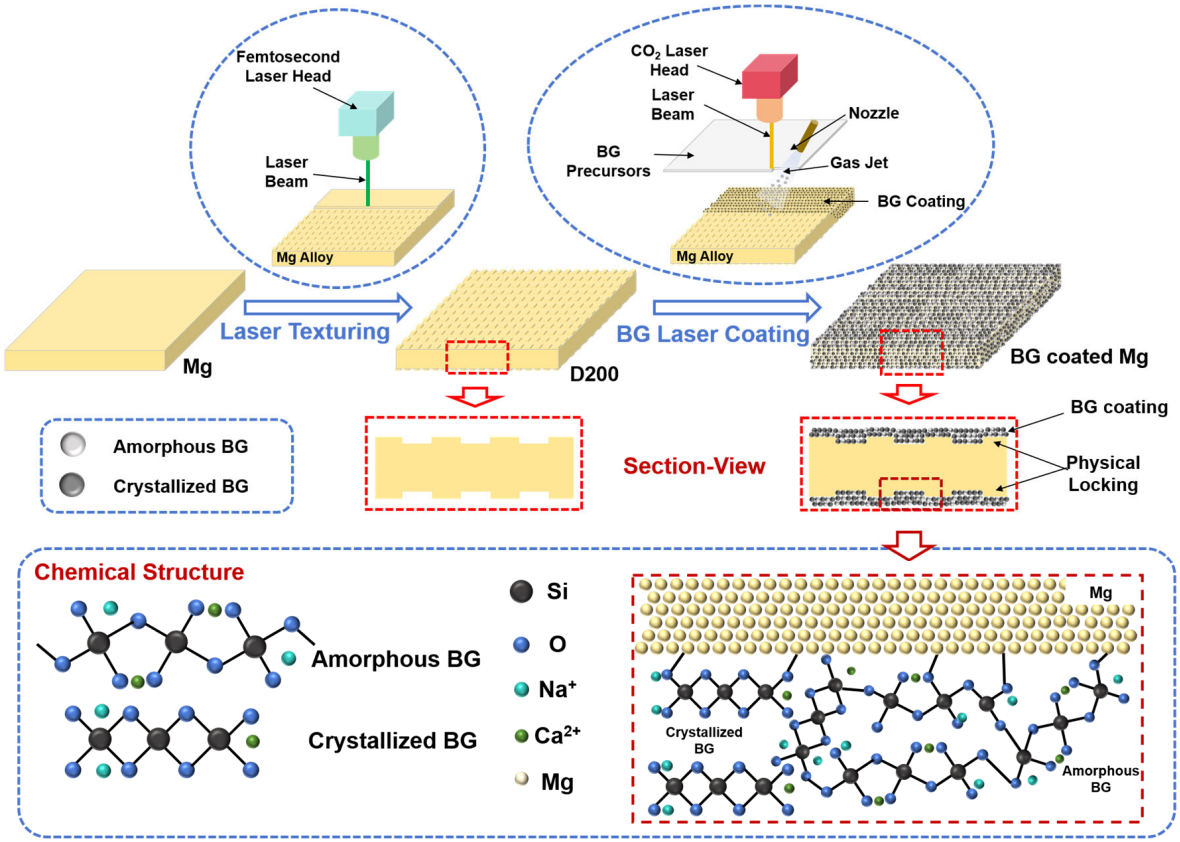


Figure 1. Illustration diagram for construction of bioactive glass coated AZ31 Mg alloy.

As the laser beam scanned along a pre-designed path, the target material absorbed the infrared radiation and locally liquefied into a high-temperature, low-viscosity glass phase. Simultaneously, a coaxial gas jet nozzle delivered a high-purity protective gas stream to exert dynamic pressure on the melt pool, overcoming the liquid surface tension to continuously blow downward molten glass micro-droplets toward the pre-textured magnesium surface. High-velocity micro-droplets impacted the preheated magnesium surface, undergoing transverse stream relaxation, stretching, and sequential overlapping to form cohesive, mechanically interlocked glass coating.

For this study, the optimal texture spacing was selected based on the results of surface coating adhesion analysis. For coating parameter optimization, the single variables were independently varied, such as the CO_2 laser output power which was set at 10, 20, and 30 W and the gas flow rate which was regulated at 10, 20, and 30 L/min; the number of repeating deposition cycles was manipulated across 1, 2, and 3 layers. All prepared samples were encoded according to the designated notation matrix (e.g., Mg-D200-A20-P20-L1) and recoded in Table 1.

Table 1. Experimental groups used for texture selection and coating optimization.

Full Designation	Short Code	Texture Spacing (μm)	Gas Flow ($L \cdot min^{-1}$)	Laser Power (W)	Layers
Mg-Control	Mg-C	/	/	/	/
Mg-D100	Mg-D100	100	/	/	/
Mg-D200	Mg-D200	200	/	/	/
Mg-D300	Mg-D300	300	/	/	/
Mg-D200-A20-P20-L1	P20/A20/L1	200	20	20	1
Mg-D200-A20-P10-L1	P10	200	20	10	1
Mg-D200-A20-P30-L1	P30	200	20	30	1
Mg-D200-A10-P20-L1	A10	200	10	20	1
Mg-D200-A30-P20-L1	A30	200	30	20	1
Mg-D200-A20-P20-L2	L2	200	20	20	2
Mg-D200-A20-P20-L3	L3	200	20	20	3

2.4. Characterization

2.4.1. Structure and Morphology for BG and Mg Alloy with Laser Treatment

X ray diffraction analysis (XRD): The crystallographic phase structures of the raw glass powder, laser-melted glass, and the as-deposited coatings before and after degradation were identified via X-ray diffraction (XRD; Ultima IV, Rigaku Corporation, Tokyo, Japan) scanned within 2θ range of 10–80° at step size of 0.02°.

Fourier transform infrared spectra (FTIR): The structural integrity and functional groups of the silicate network were characterized using Fourier-Transform Infrared Spectroscopy (FTIR; Nicolet iS5, Thermo Fisher Scientific Inc., Waltham, MA, USA) driven in attenuated total reflectance (ATR) mode over a wavenumber spectrum of 400–4000 cm^{-1} with resolution of 4 cm^{-1}.

X-ray photoelectron spectroscopy (XPS): Surface chemical valence states and cross-interface electronic elements for the typical specimens were scrutinized via X-ray photoelectron spectroscopy (XPS; AXIS Ultra DLD, Kratos Analytical Co., Ltd., Manchester, UK) using an aluminum mono-Ka X-ray source (1486.6 eV) with pass energy of 20 eV and a take-off angle of 45°.

Surface morphology observation: The surface of the Mg alloy pellets after laser surface texturing was examined using an optical microscope (RH-2000, Hirox Co., Ltd., Tokyo, Japan). For surface analysis, the front surface and cross-sectional microstructures were captured using scanning electron microscope (FE-SEM; Sigma 500, Carl Zeiss Microscopy GmbH, Jena, Germany). Cross-interface mass transport and elemental interdiffusion profiles (Mg, O and Si) were mapped using energy-dispersive X-ray spectroscopy (EDS) line-scan and area-mapping modes.

Contact angle: Static water contact angles were evaluated at room temperature via the sessile drop method using a Theta Lite optical tensiometer (Theta Lite, Biolin Scientific AB, Gothenburg, Sweden). Droplets of deionized water were dispensed onto the specimen surfaces, and specialized image analysis software was used to determine the contact angles from five distinct locations per group.

2.4.2. Coating Adhesion Evaluation

The mechanical attachment quality and interfacial adhesion of the bioactive glass coatings on the Mg alloy substrates were appraised using a pressure-sensitive tape test

according to the ASTM D3359-09 standard [19]. Standard cross-hatch grid patterns comprising six parallel cuts in each orthogonal direction were inscribed through the coating layer to penetrate the underlying substrate using a diamond-tipped stylus. A piece of tape was pressed over a scribed grid pattern with six cuts in each direction and then removed. The percentage of coating desquamation and lattice detachment within the grid area was recorded via optical microscopy and classified across an ordinal adhesion scale from 0B (highest peeling >65%) to 5B (zero delamination, 0%).

2.4.3. Electrochemical Corrosion Testing

The transient electrochemical corrosion kinetics and protection efficiency of the specimens were investigated using an electrochemical workstation (CHI660C, Shanghai Chenhua Instrument Co., Ltd., Shanghai, China) in standard simulated body fluid (SBF) maintained at physiological homeostasis temperature of 37 °C. A conventional three-electrode glass cell was configured using the processed magnesium samples (with exposed reaction area of 1 cm^2 as the working electrode, a platinum plate as the auxiliary electrode, and saturated Ag/AgCl electrode as the reference electrode. Prior to signal acquisition, the working electrode was immersed in the SBF electrolyte for 1 h to achieve stable open-circuit potential (OCP). Tafel curves were recorded by scanning the potential from −3 V to +1 V relative to the OCP at a linear scanning velocity of 0.05 Vs^{-1}. Corrosion potentials (E_{corr}) and corrosion current densities (I_{corr}) were mathematically determined via Tafel region extrapolation. Polarization resistance (R_p) was subsequently derived using the Stern–Geary method:

$$R_p = \frac{\beta_a \cdot \beta_c}{2.303 \cdot I_{corr} \cdot (\beta_a + \beta_c)} \quad (1)$$

where β_a and β_c represent the anodic and cathodic Tafel slopes, extracted from the potentiodynamic polarization curves by applying the Tafel region extrapolation method.

2.4.4. SBF Immersion, Hydrogen Evolution, and Mass Loss Measurements

Long-term degradation was evaluated by immersing specimens in 50 mL of SBF in high-density polyethylene bottles maintained at 37 °C. The SBF medium was completely refreshed every 3 days to maintain stable physiological ion concentrations. Interfacial pH variations were monitored at regular intervals using a digital pH meter (SevenExcellence S400-K, Mettler-Toledo GmbH, Greifensee, Switzerland).

For mass loss quantification, specimens retrieved at designated time points (1, 3, 5, 7, 14, and 28 days) were immersed in a chromic acid cleaning solution (200 g/L) with 10 g/L $AgNO_3$ to completely strip surface corrosion products. The cleaned pellets were rinsed ultrasonically in an acetone bath for 2 min, washed with deionized water, and dried under gaseous nitrogen. The mass loss percentage was computed using the following equation:

$$w = \frac{m_0 - m_1}{m_0} \times 100\% \quad (2)$$

where w is the mass loss rate, and m_0 and m_1 represent the sample weights measured before immersion and after product removal, respectively. Spontaneous hydrogen evolution was collected continuously using an inverted funnel-buret system. Post-immersion surfaces were microstructurally evaluated via optical microscope (RH-2000, Hirox Co., Ltd., Tokyo, Japan) and a scanning electron microscope (FE-SEM; Sigma 500, Carl Zeiss Microscopy GmbH, Jena, Germany) to confirm calcium-phosphate mineral deposition.

2.4.5. In Vitro Cytocompatibility and Osteogenic Evaluation

Cell culture: Mouse preosteoblasts (MC3T3-E1 Subclone 14, catalog no. CL-0378, Procell Life Science & Technology Co., Ltd., Wuhan, China) were cultured in specified complete growth medium within a humidified atmosphere containing 5% CO_2 at 37 °C. The culture medium was routinely replenished every 48 h. Upon attaining approximately 90% cellular confluence, the monolayer was detached and subcultured utilizing a 0.25% trypsin-EDTA solution.

Cell proliferation and viability assay: In compliance with ISO 10993-5 standard [20] protocols, cellular proliferation and viability were quantitatively evaluated using the Cell Counting Kit-8 (CCK-8; Dojindo Laboratories, Kumamoto, Japan). To prepare conditioned leachates, individual specimens were completely immersed in 2.5 mL of sterile culture medium at 37 °C for 24 h. The resulting extracts were meticulously harvested and subsequently used to treat pre-seeded confluent cell monolayers over further exposure periods (24 and 48 h). Cells cultured on standard tissue culture plates (TCP) with fresh basal medium served as the control group. Following exposure, cell viability was assayed at both the 24 and 48 h time points by adding 10 µL of the colorimetric CCK-8 solution into each well, followed by a 3 h incubation period. The absorbance was recorded at a primary wavelength of 450 nm alongside a reference wavelength of 630 nm using a multimode microplate reader (Infinite M200 PRO, Tecan Austria GmbH, Grödig, Austria). All optical density (OD) readings were normalized against the corresponding Day 1 baseline values of each group.

Alkaline phosphatase (ALP) activity: As an early-stage biochemical hallmark of osteogenic differentiation, ALP expression was assessed through both qualitative and quantitative approaches. Qualitative visualization of ALP synthesis was conducted using a BCIP/NBT chromogenic staining kit according to the manufacturer's instructions. For quantitative determination, the total enzymatic activity was quantified and normalized to the intracellular protein content, expressed as $U \cdot mg^{-1}$, using a standardized ALP assay kit.

Live/Dead cell staining: The viability and spatial distribution of cells cultured on the specimens were monitored at 24 and 48 h post-seeding via a LIVE/DEAD Viability/Cytotoxicity Kit (Thermo Fisher Scientific Inc., Waltham, MA, USA). Briefly, after aspirating the culture medium, the cell-seeded constructs were rinsed thrice with phosphate-buffered saline (PBS). A fluorogenic staining solution was freshly prepared by incorporating 5 µL of Calcein-AM and 20 µL of Ethidium Homodimer-1 into 10 mL of Dulbecco's PBS. Each specimen was submerged in 500 µL of the staining reagent and incubated at ambient temperature for 30 min in the dark. Following three subsequent PBS washes to remove background fluorophores, the fluorescently labeled cells were immediately observed under an inverted fluorescence microscope (Eclipse Ti2, Nikon Corporation, Tokyo, Japan).

2.5. Statistical Analysis

All statistical analyses were conducted using GraphPad Prism 9 (GraphPad Software, LLC, Boston, MA, USA), and the data normality was performed using one-way ANOVA followed by Tukey's post hoc test for homoscedastic data. Data are presented as mean ± SD from three biological and three technical replicates (n = 3), where * $p < 0.05$, ** $p < 0.01$, *** $p < 0.001$ were significant difference levels, and the error bars on all data represent the standard deviation.

3. Results and Discussion

3.1. Suspended-Target Coating Process

Figure 1 illustrates the two-step suspended-target coating process developed to reduce direct thermal loading on the AZ31 substrate during bioactive glass deposition. The

periodic intersecting grooves were first fabricated on the magnesium surface using the femtosecond laser, with the D200 pattern serving as the optimized anchoring structure. The short pulse duration confined material removal to the near-surface region and limited heat accumulation in the bulk substrate [21]. Then, the continuous-wave CO_2 laser was focused on the upper surface of a suspended 45S5 glass pellet to generate localized molten zone. Under the action of a coaxial gas stream, the molten glass was fragmented into droplets and transported toward the textured Mg substrate, where the droplets spread, filled the laser-generated grooves, and solidified [22]. This groove-filling behavior produced the mechanically interlocked interface and improved coating attachment compared with deposition on the smooth magnesium surface.

3.2. Texture-Dependent Wettability and Adhesion

XRD patterns of Mg-C and Mg-D200 were dominated by reflections of hexagonal α-Mg phase. Reflections located at approximately 2θ = 32.2°, 34.4°, 36.6°, 47.8°, 57.5°, 63.2°, and 68.7° were assigned to (100), (002), (101), (102), (110), (103), and (112) planes, respectively [23]. For further comparison, no additional crystalline phase was resolved after femtosecond-laser texturing within the detection limit of current XRD measurements. Crystallite size of AZ31D substrate was not estimated from XRD peak broadening because measured reflections were sharp and originated from bulk polycrystalline substrate. Moreover, instrumental broadening was not independently calibrated, and preferred orientation and residual strain could have contributed to measured peak widths. Scherrer-derived values under these conditions would represent uncertain coherent diffraction-domain sizes rather than metallographic grain sizes. Results of FTIR spectra likewise showed no distinct new absorption band after texturing. These results indicated that femtosecond-laser treatment primarily changed surface morphology without producing detectable bulk phase transformation. Surface wettability, however, was strongly dependent on grid spacing (Figure 2c). Contact angle of Mg-C was approximately 95°, whereas values of Mg-D100 and Mg-D300 increased to approximately 145° and 131°, respectively. By contrast, contact angle of Mg-D200 decreased to approximately 18°, indicating markedly improved surface wettability. Such non-monotonic behavior was likely associated with spacing-dependent liquid penetration into textured grooves. Closely spaced grooves on Mg-D100 may have retained interfacial air and promoted Cassie–Baxter-like wetting, while 200 μm spacing appeared to facilitate liquid entry into groove networks and produce Wenzel-like wetting [24]. Since contact angle can also be affected by surface chemistry, roughness, and residual contamination, this explanation should be regarded as being consistent with observed results rather than direct confirmation of wetting state.

Coating adhesion showed a similar dependence on texture spacing (Figure 2d). Mg-D200 was assigned Adhesion Class 4, compared with Class 1 for Mg-C, Class 2 for Mg-D100, and Class 3 for Mg-D300. Surface and cross-sectional SEM images (Figure 2e) provided structural support for this trend. On Mg-C, substrate boundary remained relatively flat and lacked geometrical anchoring sites. On Mg-D200, deposited glass was observed to extend into laser-generated grooves and solidify around textured features, thereby increasing interfacial contact area and producing mechanical interlocking [25]. Penetration of molten glass was likely assisted by improved wettability of Mg-D200 surface, while groove filling reduced interfacial voids and restricted coating separation during tape testing. Taken together, these results identified 200 μm grid spacing as the most suitable texture for subsequent glass deposition.

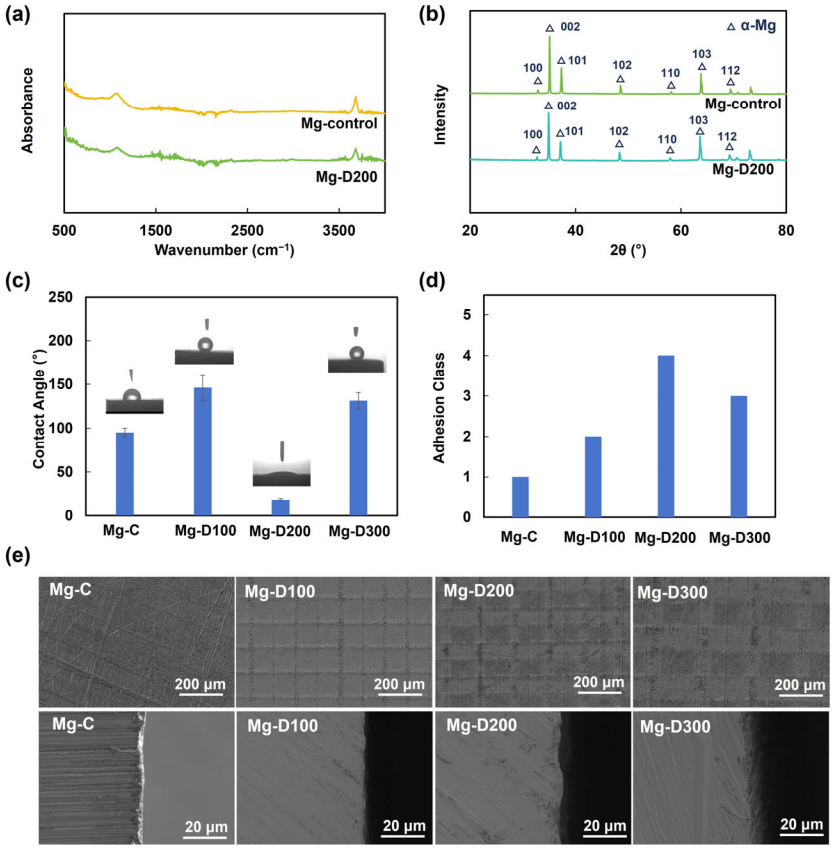


Figure 2. Effect of femtosecond-laser grid spacing on substrate structure, wettability, and coating adhesion. (**a**) FTIR spectra, (**b**) XRD patterns with indexed α-Mg reflections, (**c**) water contact angle, (**d**) coating adhesion, and (**e**) SEM image of representative surface and cross-sectional morphologies.

3.3. Coating Phase and Surface Chemistry

Phase evolution during laser processing was examined by XRD (Figure 3a). Raw 45S5 BG powder showed broad diffuse scattering between 2θ = 20° and 35°, indicating a predominantly amorphous structure. After CO_2 laser melting and solidification, multiple crystalline reflections were detected and assigned to $Na_2CaSi_3O_8$ according to reference diffraction data. Deposited coating retained a broad amorphous background together with $Na_2CaSi_3O_8$ reflections, confirming coexistence of amorphous and partially crystallized silicate phases. Reflections assigned to α-Mg were also detected in coated specimens because X-ray penetration depth extended through coating to underlying AZ31D substrate. BG coating was therefore considered to contain an amorphous matrix with dispersed, partially crystalline α-Mg domains rather than a fully crystallized glass–ceramic structure [26]. Such phase retention was likely related to rapid cooling after droplet impact, which restricted further growth of crystalline domains [27]. However, cooling rate was not measured directly and was therefore not quantified.

FTIR results supported this interpretation (Figure 3b). A broad absorption band located at approximately 1000~1040 cm^{-1} was retained in BG powder, laser-treated glass, and deposited coating and was assigned mainly to asymmetric stretching of Si–O bonds within silicate tetrahedra. Bands near 750 and 460 cm^{-1} were attributed to symmetric stretching and bending of Si–O–Si linkages, respectively. In deposited coating, an additional shoulder located at approximately 860~880 cm^{-1} was observed. This feature was consistent with increased structural ordering of silicate units and agreed with partial crystallization detected by XRD, although direct assignment to specific wollastonite-like units should be treated cautiously without complementary structural analysis [28]. Partial crystallization in-

creased structural ordering of laser-treated glass, while substantial amorphous fraction was retained after deposition. Crystalline $Na_2CaSi_3O_8$ domains may contribute to structural stability of coating, whereas the amorphous silicate matrix remains more available for ion exchange and subsequent calcium-phosphate mineralization. Nevertheless, non-monotonic contact-angle variations among laser-power, gas-flow, and deposition-cycle groups could not be explained by phase composition alone. Surface porosity, droplet coalescence, connected gaps, and exposure of Na- and Ca-containing glass components were considered more direct contributors to observed wettability. Phase structure and surface morphology therefore acted together, but their individual contributions could not be separated using current measurements.

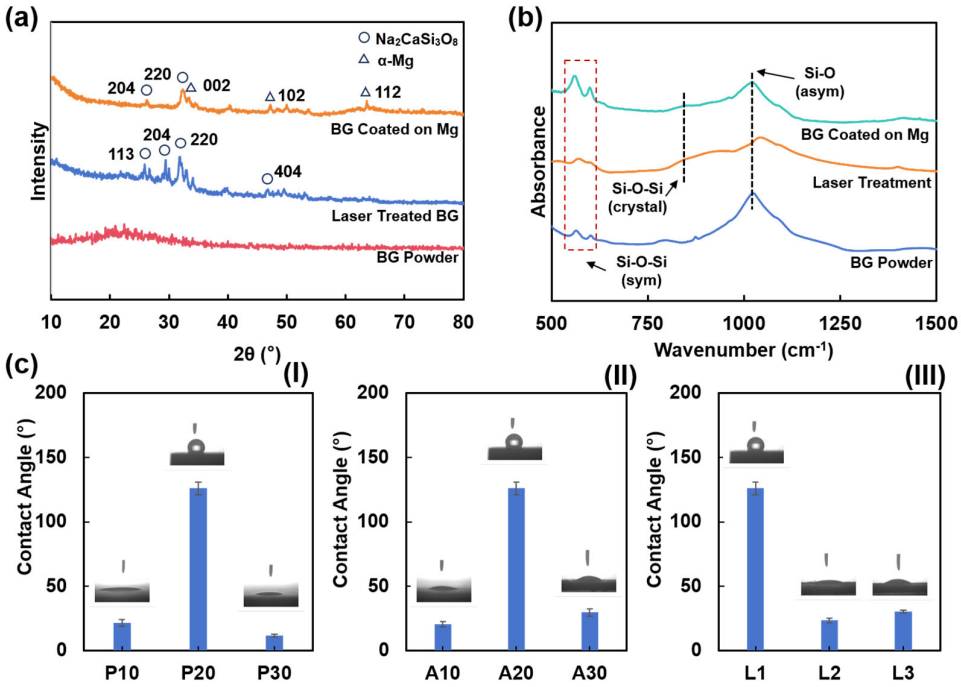


Figure 3. Chemical structure and surface wettability for Mg alloy after BG coating. (**a**) XRD patterns of 45S5 powder, laser-treated glass, and deposited coating, (**b**) ATR-FTIR spectra, and (**c**) contact angles and representative sessile-droplet images for (I) the laser-power series, (II) the gas-flow-rate series, and (III) the deposition-cycle series.

Surface wettability varied non-monotonically with processing conditions (Figure 3c). For laser-power series, P20/A20/L1 showed a contact angle of approximately 125°, whereas values measured for P10 and P30 decreased below 30°. At 10 W, incomplete melting and insufficient coalescence produced loosely packed particles and interconnected gaps. At 30 W, excessive thermal input promoted volatilization, local ejection, and irregular surface features. Both conditions increased surface heterogeneity and provided pathways for rapid water penetration, although underlying wetting response was likely governed by combined effects of roughness, porosity, and surface chemistry rather than roughness alone.

Similar behavior was observed for gas-flow series. Contact angle remained approximately 125° at 20 L·min^{-1} but decreased substantially for A10 and A30. At 10 L·min^{-1}, limited aerodynamic shear resulted in deposition of incompletely dispersed glass agglomerates. At 30 L·min^{-1}, accelerated convective cooling likely caused partial solidification before droplet impact, thereby limiting spreading and producing a porous surface. Both morphologies favored liquid infiltration through connected surface defects. Increasing deposition cycles from L1 to L2 and L3 also reduced contact angle from approximately 125° to 20°~30°. Secondary deposition appeared to fill part of the initial track-junction network and altered exposure of Na- and Ca-containing glass phases at the outer surface.

A resulting increase in polar surface sites, together with changes in microstructure, was considered responsible for improved wettability. Since contact angles remained above 10°, these surfaces were described as strongly hydrophilic rather than superhydrophilic.

Surface chemical states of Mg-C, Mg-D200, and P20/A20/L1 specimens were further examined by high-resolution XPS (Figure 4). In the Mg_{1S} core level spectra, the unpatterned Mg-C substrate exhibited a prominent oxidation reflection peak centered at approximately 1304.3 eV. Following femtosecond-laser texturing, the Mg_{1S} intensity of the Mg-D200 sample rose significantly. This peak enhancement is attributed to the thermal ablation processing in air-accelerating native oxidation to yield a surface enriched with structured metal oxides/hydroxides. Remarkably, upon the deposition of the 45S5 glass coating, the Mg_{1S} signal of the A20/P20/L1 cohort collapses to a negligible baseline level. This rapid signal attenuation establishes that the underlying, reactive magnesium substrate is conformally sealed and dynamically isolated by the thick cladded glass matrix layer.

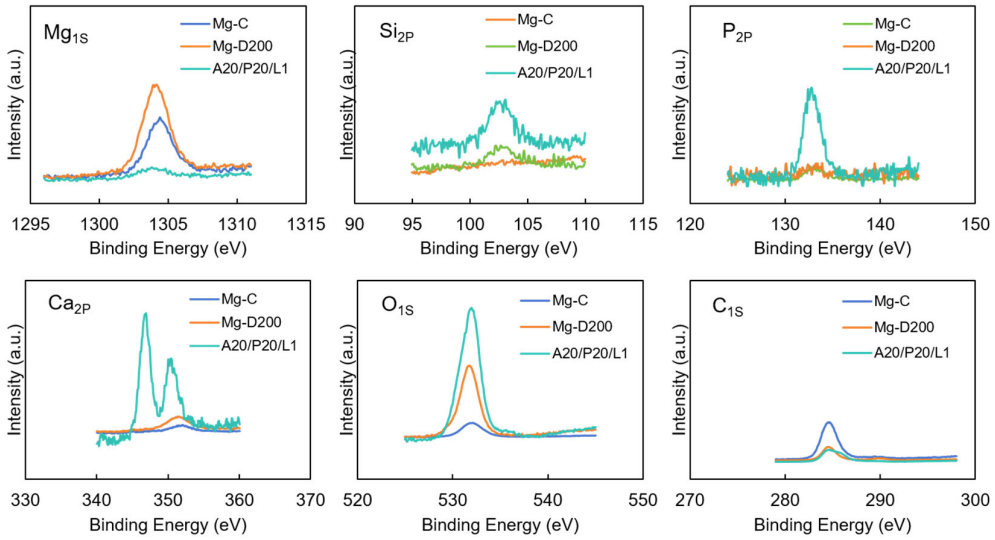


Figure 4. High-resolution XPS core level spectra of element of Mg, Si, P, Ca, O, and C obtained from the surfaces of the magnesium alloy with different treatment.

Signals from glass-network constituents were detected only after coating deposition. The Si_{2P} and P_{2P} core level spectra, which register zero background for both the Mg-C and Mg-D200 baselines, exhibit well-defined and asymmetric peak profiles centered at 102.5 eV and 132.8 eV, respectively, on the A20/P20/L1 coated surface. These peaks confirm the structural integrity of the amorphous-crystalline silicate network skeleton. Simultaneously, the high-resolution Ca_{2P} spectrum splits into two distinctive doublet peaks corresponding to Ca_{2P} 1/2 and Ca_{2P} 3/2 spin–orbit couplings centered at 350.5 eV and 346.8 eV, providing solid spectroscopic proof of chemical bonding inside a stable calcium silicate structure. In parallel, the single-layer deposition triggers an increase in the O_{1S} peak intensity at 531.8 eV, representing the covalent bridging oxygen bonds (Si-O-Si and P-O-Si) within the glass, while the adventitious C_{1S} peak at 284.6 eV remains suppressed [29]. This complete chemical profiling demonstrates that the spatial thermal decoupling strategy successfully deposits a highly pure, bioactive function for the silicate barrier on the magnesium surface, avoiding any metallic out-diffusion or elemental cross-contamination from the substrate.

3.4. Process-Dependent Morphology of BG Coating

The macroscopic surface topographies, cross-sectional configurations, and quantitative thickness distribution mapping of the cladded coatings are systemically evaluated in Figures 5, S2 and S3 as a function of the single-factor parameters, including laser power

P(x), gas flow rate A(y), and cyclical layer build-up L(z). Macrostructural visual inspection via optical photography (Figure S2) demonstrates that the untextured Mg-C substrate features an isotropic metallic luster, while the femtosecond-laser-textured Mg-D200 substrate displays a highly uniform orthogonal grid network. Upon the deposition of the ex situ cladded glass coatings, the continuous, dense ceramic blanket coverage is realized across all coated parameter variations. However, quantitative cross-sectional determinations (Figures 5 and S3) uncover that the terminal coating thickness follows a highly sensitive, non-monotonic response to both processing thermal energy and aerodynamic gas momentum, while expanding monotonically with cyclical layer accumulation [30].

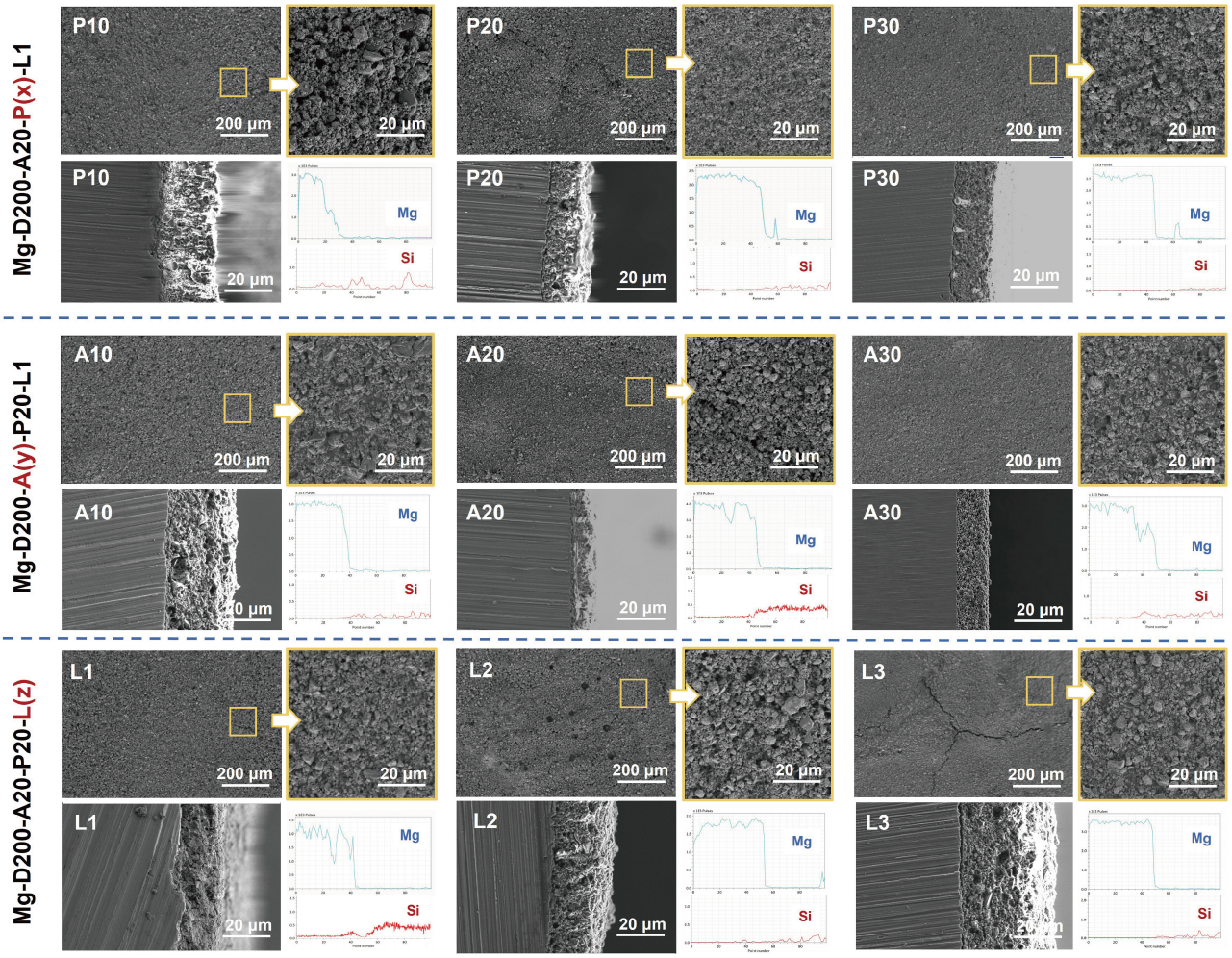


Figure 5. SEM image and EDS mapping for surface and cross-sectional morphologies of coatings prepared at different laser powers, gas-flow rates, and deposition-cycle numbers.

Regarding the laser power parameter series P(x), P10 produced a relatively thick coating of 36.2 ± 1.1 μm. Cross-sectional images, however, showed incomplete particle coalescence and numerous interparticle voids, indicating that 10 W was insufficient for stable melting and spreading of glass feedstock. At 20 W, a more continuous and compact layer was obtained, with a thickness of 25.5 ± 1.8 μm. This condition appeared to provide better balance between glass melting, droplet transport, and surface spreading. When laser power was increased to 30 W, coating thickness decreased to 12.3 ± 0.8 μm. Irregular surface features and reduced deposited volume suggested that excessive thermal input promoted material loss through volatilization or melt ejection. Consequently, physical coverage provided by P30 was more limited than that obtained at 20 W.

Concerning the gas flow rate parameters A(y), the aerodynamic jet kinetics determine a classic trade-off between molten pool shearing and flight-line cooling rate [31]. The low gas flow of 10 L·min^{-1} (A10) delivered inadequate shear stress to atomize the target melt pool, yielding a loose, un-melted macro-particle accumulation with exaggerated layer thickness of 38.5 ± 1.4 μm (Figure S3). When optimized to 20 L·min^{-1} (A20), the gas jet effectively shears the low-viscosity non-Newtonian melt into micro-droplets, producing a highly uniform, dense coating blanket with a standard thickness of 25.5 ± 1.8 μm. Conversely, an excessive flow of 30 L·min^{-1} (A30) induces rapid convective cooling of the droplets during flight. The micro-particles solidify prematurely before they can relax and conformally wet the micro-grooves, resulting in a significantly thinner and loose layer with a thickness of only 15.1 ± 1.6 μm.

For the cyclical-layer number series L(z), coating thickness increased progressively with deposition cycles. The coating thickness of the L1 specimen was measured at 25.5 ± 1.8 μm and contained small gaps near overlapping deposition tracks. After the second deposition cycle, these discontinuities were largely filled, and a dense layer with a thickness of 50.5 ± 2.1 μm was formed. Such defect filling was considered responsible for improved barrier continuity of L2 coating. Further deposition increased thickness to 77.8 ± 1.3 μm for L3; pronounced surface cracks were observed in optical and cross-sectional images. This crack formation was attributed to accumulation of residual stress caused by repeated thermal cycling and thermal-expansion mismatch between glass layer and magnesium substrate [32]. These cracks could provide preferential pathways for electrolyte penetration, explaining why greater thickness did not necessarily lead to better corrosion protection.

3.5. Electrochemical Corrosion Behavior

Electrochemical behavior of Mg-C, Mg-D200, and BG-coated specimens was examined in SBF at 37 °C (Figure 6, Table 2, and Figure S4). Potentiodynamic polarization curves provided quantitative support for this interpretation (Figure 6a and Table 2). Mg-C showed corrosion current density of 8.72 × 10^{-4} A·cm^{-2} and polarization resistance of 1.21 × 10^{3} Ω·cm^{2}. After femtosecond-laser texturing, I_{corr} of Mg-D200 increased slightly to 1.01 × 10^{-3} A·cm^{-2}. Increased electrochemically accessible area and enhanced electrolyte wetting may have contributed to this change. All BG-coated specimens showed lower corrosion current densities than uncoated groups, although protection varied with processing condition. The best response was obtained for the L2 specimen, with I_{corr} of 5.33 × 10^{-6} A·cm^{-2} and R_p of 1.39 × 10^{5} Ω·cm^{2}. Relative to Mg-C, corrosion current density was reduced by approximately 163-fold, while polarization resistance increased by approximately 116-fold. These results showed that double-layer deposition provided the most effective electrochemical barrier within the tested parameter range, mainly because defects in the primary layer had been sealed without extensive cracking associated with L3 [33].

Differences in interfacial resistance were also reflected in Nyquist plots (Figure 6b). Capacitive arcs of coated specimens were substantially larger than those of Mg-C and Mg-D200, indicating increased resistance to charge transfer and electrolyte penetration [34]. Performance varied non-monotonically with processing parameters. P20, A20, and particularly L2 produced largest impedance responses, whereas specimens of P10, P30, A10, A30, and L3 showed smaller arcs. This trend closely followed morphology of deposited layers. For the L2 specimen, a secondary deposition filled many gaps retained in L1 and increased diffusion distance for water and ions of Cl^{-} through coating [35]. By contrast, cracks generated during the third deposition cycle provided shorter pathways for electrolyte transport, offsetting benefit expected from increased thickness [36]. Therefore, corrosion

protection was governed primarily by coating continuity and defect connectivity rather than thickness alone.

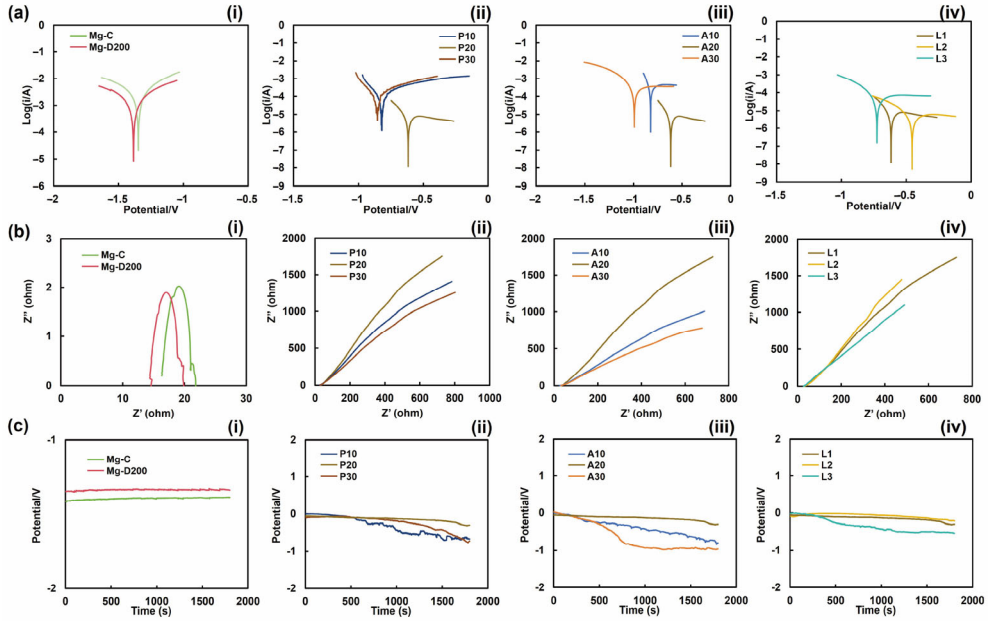


Figure 6. Electrochemical behavior in SBF at 37 °C. (**a**) Potentiodynamic polarization curves, (**b**) Nyquist plots and (**c**) open-circuit potential as a function of time for (**i**) Mg-C and D200, (**ii**) laser-power groups, (**iii**) gas-flow groups and (**iv**) layer-number groups.

Table 2. Electrochemical parameters in SBF at 37 °C.

Sample Code	Ecorr (V)	Icorr ($\times 10^{-4}$ A·cm^{-2})	Ba (mV·dec^{-1})	Bc (mV·dec^{-1})	Rp ($\times 10^{3}$ Ω·cm^{2})
Mg-Control	−1.35 ± 0.07	8.72 ± 0.44	4.61 ± 0.23	5.08 ± 0.25	1.21 ± 0.06
Mg-D200	−1.38 ± 0.07	10.13 ± 0.51	4.76 ± 0.24	4.96 ± 0.23	1.04 ± 0.05
P20/A20/L1	−0.62 ± 0.04	0.12 ± 0.01	7.41 ± 0.52	2.31 ± 0.16	66.41 ± 4.65
P10	−0.82 ± 0.07	0.82 ± 0.03	8.15 ± 0.33	3.94 ± 0.17	14.13 ± 0.56
P30	−0.85 ± 0.04	0.96 ± 0.05	7.93 ± 0.79	4.20 ± 0.42	12.42 ± 1.24
A10	−0.93 ± 0.05	1.80 ± 0.09	27.23 ± 1.36	1.51 ± 0.08	34.64 ± 0.17
A30	−0.99 ± 0.05	2.60 ± 0.13	6.51 ± 0.33	2.34 ± 0.12	2.88 ± 0.14
L2	−0.46 ± 0.03	0.05 ± 0.01	6.27 ± 0.44	2.33 ± 0.16	139.25 ± 9.71
L3	−0.72 ± 0.06	0.48 ± 0.02	6.75 ± 0.27	2.61 ± 0.11	17.13 ± 0.68

During OCP monitoring (Figure 6c), Mg-C and Mg-D200 remained at relatively negative potentials, indicating that both surfaces were maintained in electrochemically active states. More positive potentials were recorded for coated groups, showing that direct interaction between electrolyte and Mg substrate had been reduced after glass deposition. Among tested conditions, the coatings for the L2 specimen could effectively seal the micro-porosity of the primary layer, creating a complex, labyrinth-like barrier that forces aggressive ions to traverse a significantly longer diffusion pathway. Conversely, the excessive thermal stress induced by the third deposition cycle (L3) leads to micro-crack propagation, which negates this barrier benefit and allows rapid electrolyte penetration. Collectively, these data confirm that the synergistic combination of laser texturing and double-layer deposition provides an optimal, predetermined degradation barrier essential for maintaining the mechanical structural integrity of AZ31 alloy.

3.6. Degradation and Surface Mineralization

Degradation behavior of Mg-C, Mg-D200, and BG-coated specimens was examined during 28-day immersion in SBF at 37 °C (Figures 7, 8, S4 and S5). Mass-loss results and solution pH changes showed clear dependence on surface condition and coating parameters. By day 28, cumulative mass losses of Mg-C and Mg-D200 reached approximately 19% and 21%, respectively (Figure 7a(i)). In both groups, solution pH increased above 10.0 during the first 7 days and approached 10.5 at later time points (Figure 7b(i)).

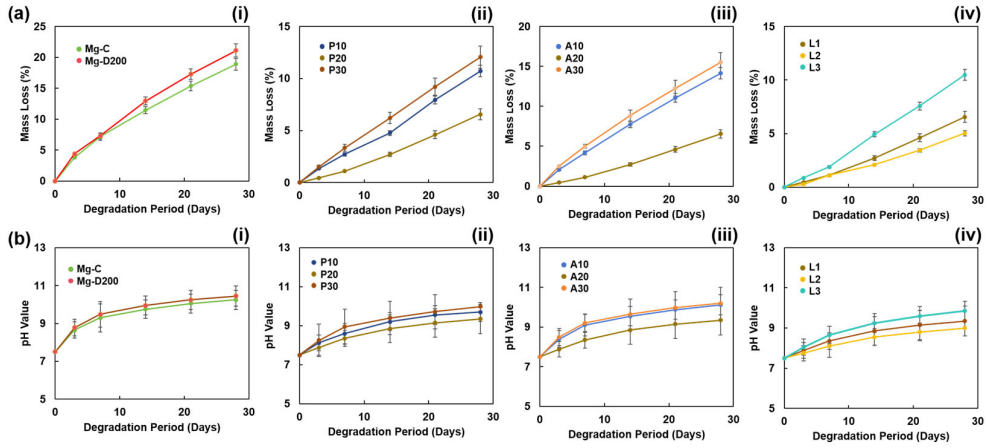


Figure 7. Degradation analysis for Mg alloy in SBF. (**a**) Mass loss and (**b**) solution pH for (**i**) Mg-C and D200, (**ii**) laser-power groups, (**iii**) gas-flow groups and (**iv**) layer-number groups.

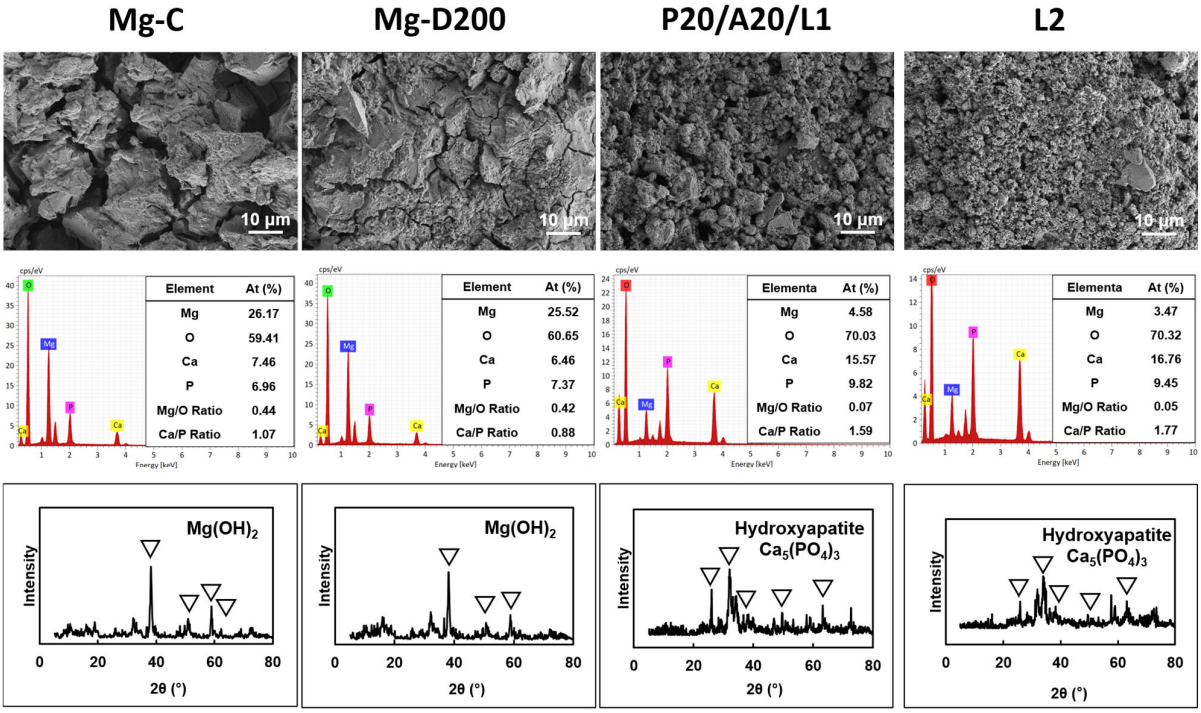


Figure 8. SEM image of surface with EDS mapping for mineralization characterization after 28 days in SBF for Mg-C, Mg-D200, P20/A20/L1 and L2.

Optical images obtained after immersion showed extensive corrosion-product accumulation, local peeling, and visible dimensional loss on Mg-C and Mg-D200 surfaces (Figure S5). Slightly greater degradation of Mg-D200 was likely related to increased exposed surface area and enhanced electrolyte penetration into laser-generated grooves. These features may have accelerated chloride-assisted destabilization of the initially formed

$Mg(OH)_2$ layer and promoted continued substrate dissolution [37]. Markedly lower mass loss and smaller pH increases were measured after BG deposition, although protection varied with processing condition.

Within laser-power and gas-flow series, P20 and A20 provided the most stable degradation profiles (Figure 7a,b). By contrast, higher mass loss and faster pH changes were recorded for P10, P30, A10, and A30. Surface SEM images collected after 28 days helped explain these differences (Figure S6). Porous regions and incompletely fused particles were retained in P10 and A10 coatings, whereas pinholes, irregular deposits, and locally discontinuous regions were observed for P30 and A30. Such defects provided preferential routes for electrolyte transport and allowed localized corrosion to develop beneath the coating. These observations also indicated that corrosion resistance was controlled less by deposited mass than by continuity of coating and connectivity of defects.

Furthermore, deposition-cycle series showed similar structure-dependent behavior (Figure 7a(iv),b(iv)). L1 provided partial protection, but gradual electrolyte penetration was still possible through gaps between overlapping deposition tracks. Lowest mass loss and most limited pH variation were obtained for L2 throughout 28-day immersion. Optical images showed that L2 coating remained largely continuous, with no obvious macroscopic delamination or extensive section loss (Figure S5). Additional deposition did not provide further improvement. L3 exhibited visible surface cracks, and degradation resistance decreased despite greater coating thickness. Crack formation was likely associated with residual stress accumulated during repeated heating and cooling, together with thermal-expansion mismatch between silicate coating and Mg substrate. Once connected, these cracks shortened the electrolyte diffusion path and reduced the barrier effect of the thick coating.

Mineral formation after 28 days was further examined by SEM, EDS, and XRD (Figure 8). Mg-C and Mg-D200 surfaces were mainly covered by loose, cracked, plate-like corrosion products. Local Ca/P atomic ratios determined by EDS were 1.07 and 0.88, respectively, while XRD patterns were dominated by Mg substrate and $Mg(OH)_2$-related reflections. In contrast, P20/A20/L1 and L2 surfaces were covered by dense aggregates with cauliflower-like morphology, which is commonly associated with calcium-phosphate deposition. Local Ca/P ratios increased to 1.59 for L1 and 1.77 for L2, approaching the stoichiometric value of hydroxyapatite (1.67). Diffraction peaks assigned to hydroxyapatite were also detected, supporting the formation of an apatite-containing mineral layer on BG-coated specimens [38,39].

Mineralization was attributed to the gradual dissolution of amorphous silicate-rich phase and subsequent release of Ca-containing species into surrounding solution. Hydrolysis of the silicate network generated surface silanol groups, which provided favorable sites for adsorption of Ca^{2+} and PO_4^{3-}. Calcium-phosphate nuclei were then formed and progressively converted into apatite-containing deposits. Besides improving surface bioactivity, deposited mineral layer may also have filled part of residual porosity and further restricted electrolyte access. Thus, long-term behavior of optimized coatings appeared to arise from combined action of initial physical barrier and subsequent surface mineralization rather than from coating thickness alone.

3.7. Degradation Mechanism Analysis

To comprehensively delineate the interfacial mass transport, localized dissolution, and dynamic biomimetic mineralization phenomena, a mechanistic degradation model for the uncoated and laser-coated systems is schematically proposed in Figure 9. For Mg-C and Mg-D200, SBF was allowed to contact Mg substrate directly, and anodic dissolution of Mg was accompanied by cathodic water reduction [40]. Resulting OH^- accumulation increased

local pH and promoted temporary formation of $Mg(OH)_2$. In chloride-containing SBF, however, this surface film remained unstable and was gradually converted into more soluble Mg^- and Cl^- containing products, allowing localized corrosion to continue. Slightly faster degradation of Mg-D200 was attributed to greater exposed area and easier electrolyte retention within laser-generated grooves. Rather than acting as protective features by themselves, grooves provided additional sites for solution access before glass deposition.

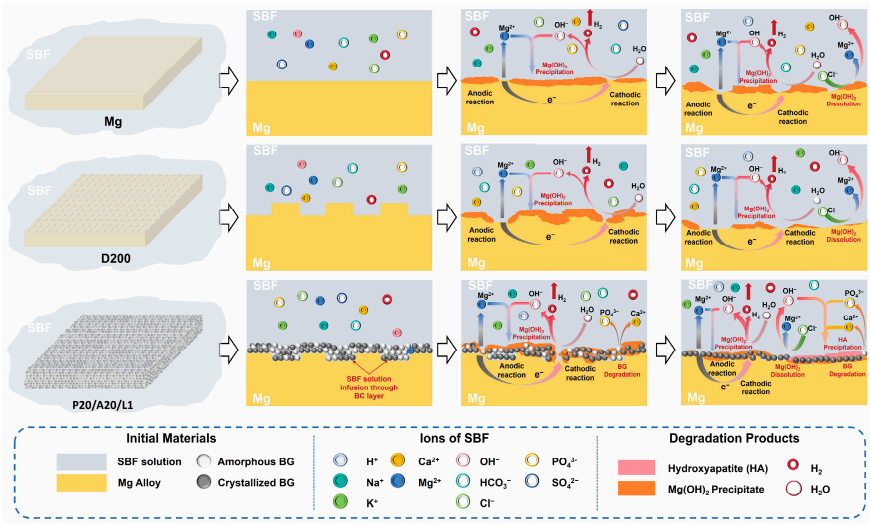


Figure 9. Proposed degradation and mineralization mechanism for Mg-C, D200 and P20/A20/L1 specimens with different surface treatment in SBF.

Different interfacial behavior was observed after suspended-target BG deposition. In representative P20/A20/L1 coating, the amorphous–partially crystalline silicate layer initially reduced direct contact between SBF and Mg substrate. Transport of H_2O and Cl^- was delayed with coating thickness and by a less connected pore network, while corrosion remained concentrated near local defects. This interpretation was consistent with lower corrosion current, higher polarization resistance, and reduced mass loss measured for coated groups. Protection was therefore considered to arise mainly from coating continuity and defect distribution, rather than from glass thickness alone.

With extended immersion, surface reactions of bioactive glass became increasingly important. Ion exchange between glass and surrounding solution released Na^+ and Ca^{2+}, while hydrolysis of Si-O--Si bonds generated Si-OH groups at the coating surface [41]. These groups provided favorable sites for Ca^{2+} adsorption and subsequent incorporation of phosphate species from SBF [42]. Calcium-phosphate deposits were then formed and gradually developed into an apatite-containing mineral layer, as supported by cauliflower-like morphology, increased Ca/P ratios, and HAp-related XRD reflections after 28 days. Mineral deposits may also have filled part of residual pores and reduced further electrolyte access. Thus, degradation control was attributed to the sequential contribution of the initial glass barrier and later calcium-phosphate mineralization. This combined response slowed Mg dissolution while producing a more favorable surface for subsequent bone-related cell activity, although direct in vivo osteoconductive performance remains to be verified [43].

3.8. Cytocompatibility and Osteogenic Response

To evaluate the in vitro cytocompatibility and osteogenic differentiation potential of the engineered surfaces, cellular responses within the specimens' culture system were dynamically monitored (Figures 10 and S6). The quantitative cell proliferation was determined using the CCK-8 assay over a 7-day incubation period (Figure 10a). While all experimental groups registered comparable baseline viability on Day 1, the proliferation

profiles diverged significantly by Day 3 and Day 7. The uncoated Mg-C and textured Mg-D200 specimens exhibited severely suppressed growth behavior, consistent with their rapid degradation rates and localized alkaline bursts. In contrast, the BG-coated specimen (P20/A20/L1 and L2) supported exponential cellular proliferation. By Day 7, the cell viability on the optimized two layers (L2) coating was significantly improved ($p < 0.001$) when compared to the uncoated baselines. This rapid proliferative expansion indicates that the stable, physiological pH environment provided by the structural barrier coating is highly conducive to long-term cellular survival and colonization.

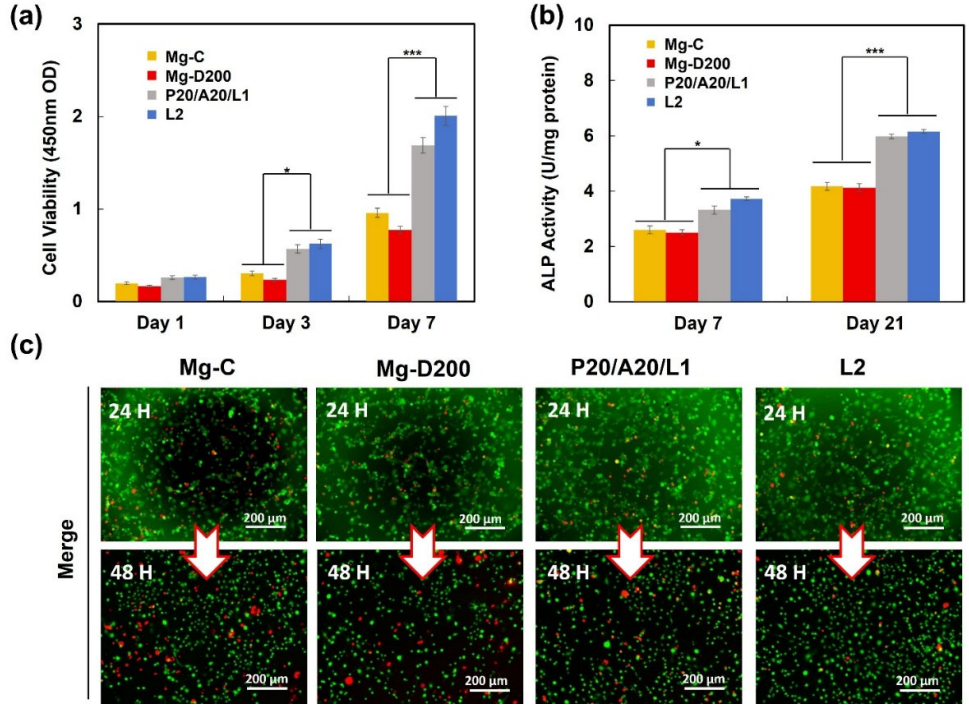


Figure 10. Evaluation of cell proliferation and osteogenic differentiation. (**a**) Quantitative analysis of cell proliferation determined by the CCK-8 assay. (**b**) Qualitative assessment of alkaline phosphatase (ALP) activity, and (**c**) fluorescence images for live/dead staining cells cultured in the specimens after 24/48 h. Statistical comparisons are indicated by brackets (* p <0.05 and *** $p < 0.001$ as determined by two-way ANOVA followed by Tukey's multiple-comparisons test).

Furthermore, the osteoinductive capacity of the modified interfaces was evaluated by quantifying alkaline phosphatase (ALP) activity (Figure 10b). For Day 7, the L1 and L2 specimens already exhibited significantly elevated ALP expression ($p < 0.05$) relative to the bare substrates (Mg-C and Mg-D200). This osteogenic enhancement became remarkably pronounced after 21 days of extended culture. The ALP activity of the coated groups, particularly the L2 architecture, surged significantly ($p < 0.001$), vastly outperforming the Mg-C and Mg-D200 groups. This profound osteogenic stimulation is driven by the intrinsic biomimetic mineralization capability of the bioactive glass matrix [44]. The controlled and sustained release of ions such as Ca^{2+} from the degrading glass network of BG coating could actively upregulate osteogenic differentiation pathways [45].

These quantitative biochemical trends are visually corroborated by the qualitative cell viability, adhesion, and distribution profiles assessed via live/dead fluorescence staining after 24 and 48 h (Figure 10c, supplemented by the separated fluorescence channels in Figure S7). The unmodified Mg-C and textured Mg-D200 substrates exhibited severe acute cytotoxicity. At 24 h, these uncoated groups displayed localized non-adherent necrotic zones. The microenvironment deteriorated further by 48 h, evidenced by restricted,

rounded cellular morphologies and a significant accumulation of dead cells emitting red fluorescence. This toxicity is directly attributed to the burst release of Mg^{2+} ions and violent hydrogen gas evolution from the uninhibited degradation of bare magnesium [46]. Conversely, the cladded coatings successfully rescued the physiological microenvironment. Both surfaces of L1 and L2 specimens promoted uniform cell attachment and robust spreading, displaying dense living cells (green fluorescence) with negligible apoptotic signals [47]. Specifically, the L2 coating exhibited the highest live cell density and optimal spreading morphology. Collectively, these in vitro results unequivocally demonstrate that the intact double-layer physical barrier transforms the initially cytotoxic magnesium surface into a highly cytocompatible and osteoinductive platform, fulfilling the rigorous biological prerequisites for advanced orthopedic implant applications.

3.9. Process Implications and Study Limitations

The results obtained in this study presented that the performance of coated AZ31 Mg alloy was determined by combined effects of surface texture and BG coating structure. No single processing parameter produced consistent improvement when increased independently. Instead, best overall response was obtained only when sufficient interfacial anchoring was achieved without introducing excessive porosity or thermal cracking.

For femtosecond-laser texturing process, it was confirmed with two different effects on Mg alloy. Before coating deposition, Mg-D200 showed slightly faster degradation than Mg-C, which was likely related to increased exposed area and easier electrolyte retention within grooves. During glass deposition, however, the same groove network provided sites for molten glass penetration and solidification. Adhesion Class of 4B obtained for Mg-D200 suggested that mechanical interlocking had been improved by this textured interface. Thus, texture itself was not protective, whilst its main benefit was realized only after grooves had been filled by deposited glass. Surface and phase analyses also indicated that suspended-target processing reduced direct thermal exposure of Mg substrate and preserved predominantly amorphous silicate structure in coating. Nevertheless, complete absence of substrate melting or elemental interdiffusion could not be established from current surface characterization alone.

During coating process, the effects of CO_2 laser power, gas flow rate and deposition cycle were also non-monotonic. The specimen of P20/A20/L1 may provide the most favorable combination of coating density, thickness, and defect control. During the second deposition cycle, gaps remaining between primary deposition tracks were largely filled, which reduced connected pathways for ions transport. However, further deposition was confirmed with a structure issue (L3 specimen) due to repeated heating and cooling indicating visible cracks, and corrosion resistance decreased. This comparison suggests that barrier performance was governed more strongly by defect connectivity than by total coating thickness.

As such, improved electrochemical stability was observed for the L2 specimen, accompanied by lower mass loss, smaller pH variation, and better MC3T3-E1 response. Based on current in vitro evidence, bioactive performance is more appropriately described as enhanced cytocompatibility and osteogenic support rather than confirmed osteoinductivity. Formation of apatite-containing deposits may also have reduced electrolyte access by partially filling residual surface defects, although direct self-sealing behavior was not monitored in real time.

Several limitations should be considered when interpreting these results. Processing conditions were screened using discrete single-factor experiments, so interactions among texture spacing, laser power, gas flow rate, and deposition cycle were not statistically resolved. Factorial design or response surface methodology would be more suitable for

defining combined processing windows. Residual stress, quantitative adhesion strength, droplet velocity, impact temperature, and in-flight solidification behavior were not measured, leaving several proposed processing mechanisms to be verified. In addition, release of alloying elements was not quantified during current immersion tests. Although continuous BG coating reduced direct contact between SBF and AZ31D substrate, localized exposure at coating defects may permit release of Al-, Zn-, and Mn-containing species. Future studies should quantify time-dependent elemental release by ICP-OES or ICP-MS and relate measured concentrations to cellular response. Furthermore, SBF immersion and static MC3T3-E1 culture represented simplified in vitro conditions. Corrosion fatigue, cyclic loading, fluid shear, protein adsorption, inflammatory response, and immune-cell regulation were not reproduced. As such, further evaluation under dynamic loading and in vivo conditions will therefore be required before long-term mechanical stability, degradation compatibility, and bone integration can be assessed.

4. Conclusions

In summary, we successfully developed and validated suspended-target laser deposition of partially crystallized 45S5 bioactive glass on femtosecond-laser-textured AZ31 Mg alloy, providing an effective strategy for improving coating adhesion, degradation control, and surface bioactivity. The 200 μm laser-textured grid provided mechanical anchoring by allowing molten glass droplets to penetrate and solidify within laser-generated grooves. Based on this interface, an optimal coating structure was obtained at 20 W laser power, 20 $L \cdot min^{-1}$ gas flow, and two deposition cycles. The first deposited layer acted as a primary corrosion barrier, while the second layer filled inter-track gaps and reduced connected defects, producing denser and more continuous glass coating. This double-layer structure reduced corrosion current density by approximately 163-fold and increased polarization resistance by approximately 116-fold compared with bare AZ31, while also limiting mass loss and pH increase during 28-day SBF immersion. Controlled dissolution of bioactive glass promoted calcium-phosphate deposition and formation of hydroxyapatite-containing mineral layer. Improved interfacial stability and surface mineralization were accompanied by enhanced MC3T3-E1 cell viability, proliferation, and ALP activity. This combined femtosecond-texturing and suspended-target laser deposition approach therefore provides a promising route for fabricating biodegradable magnesium implants with improved corrosion resistance and osteogenic response, particularly for load-bearing applications such as spinal fusion.

Supplementary Materials: The following supporting information can be downloaded at: https://www.mdpi.com/article/10.3390/coatings16080958/s1. Figure S1: SEM image of as received bioactive glass; Figure S2: Macroscopic appearance of Mg-Control, D200 and coated specimens before immersion; Figure S3: Thickness of coatings for Mg substrate with different coating process; Figure S4: Comparison of Ecorr and Icorr for the electrochemical test groups; Figure S5: Optical images of specimens after 7 and 28 days of SBF immersion; Figure S6: SEM images of BG coated specimens P10, P30, A10 and A30 after 28 days of SBF immersion; Figure S7: Separated images for Live and Dead staining fluorescence images of cells cultured in the hydrogel after 24/48 h.

Author Contributions: C.Z.: Writing—original draft, investigation, resources. Y.W.: methodology, data curation. Z.S.: Supervision, conceptualization. L.L.: Writing—review and editing, supervision. All authors have read and agreed to the published version of the manuscript.

Funding: This research was partially funded by Ningbo Key Projects of Science and Technology, grant number 2023Z192, International Sci-tech Cooperation Projects under the "Innovation Yongjiang 2035" Key R&D Programme, grant number 2024H014, and Ningbo Yongjiang Young talent sub-project Programme grant number 2022A-147-G.

Data Availability Statement: Data will be shared upon request.

Conflicts of Interest: The authors declare no conflicts of interest.

Abbreviations

The following abbreviations are used in this manuscript:

BG	Bioactive Glass
Mg	Magnesium

References

1. Luo, Y.; Wang, J.; Ong, M.T.Y.; Yung, P.S.-H.; Wang, J.; Qin, L. Update on the research and development of magnesium-based biodegradable implants and their clinical translation in orthopaedics. *Biomater. Transl.* **2021**, *2*, 188–196. [CrossRef]
2. Wang, J.L.; Xu, J.K.; Hopkins, C.; Chow, D.H.K.; Qin, L. Biodegradable magnesium-based implants in orthopedics—A general review and perspectives. *Adv. Sci.* **2020**, *7*, 1902443. [CrossRef] [PubMed]
3. Shan, Z.; Xie, X.; Wu, X.; Zhuang, S.; Zhang, C. Development of degradable magnesium-based metal implants and their function in promoting bone metabolism (A review). *J. Orthop. Transl.* **2022**, *36*, 184–193. [CrossRef] [PubMed]
4. Zhang, Y.; Xu, J.; Ruan, Y.C.; Yu, M.K.; O'Laughlin, M.; Wise, H.; Chen, D.; Tian, L.; Shi, D.; Wang, J.; et al. Implant-derived magnesium induces local neuronal production of CGRP to improve bone-fracture healing in rats. *Nat. Med.* **2016**, *22*, 1160–1169. [CrossRef] [PubMed]
5. Han, H.S.; Jun, I.; Seok, H.K.; Lee, K.S.; Lee, K.; Witte, F.; Mantovani, D.; Kim, Y.C.; Glyn-Jones, S.; Edwards, J.R. Biodegradable Magnesium Alloys Promote Angio-Osteogenesis to Enhance Bone Repair. *Adv. Sci.* **2020**, *7*, 2000800. [CrossRef] [PubMed]
6. Shen, J.; Chen, B.; Zhai, X.; Qiao, W.; Wu, S.; Liu, X.; Zhao, Y.; Ruan, C.; Pan, H.; Chu, P.K.; et al. Stepwise 3D-spatio-temporal magnesium cationic niche: Nanocomposite scaffold mediated microenvironment for modulating intramembranous ossification. *Bioact. Mater.* **2021**, *6*, 503–519. [CrossRef] [PubMed]
7. Mei, D.; Lamaka, S.V.; Lu, X.; Zheludkevich, M.L. Selecting medium for corrosion testing of bioabsorbable magnesium and other metals—A critical review. *Corros. Sci.* **2020**, *171*, 108722. [CrossRef]
8. Kuah, K.X.; Wijesinghe, S.; Blackwood, D.J. Toward understanding in vivo corrosion: Influence of interfacial hydrogen gas build-up on degradation of magnesium alloy implants. *J. Biomed. Mater. Res. A* **2023**, *111*, 60–70. [CrossRef] [PubMed]
9. Singh, N.; Batra, U.; Kumar, K.; Ahuja, N.; Mahapatro, A. Progress in bioactive surface coatings on biodegradable Mg alloys: A critical review towards clinical translation. *Bioact. Mater.* **2023**, *19*, 717–757. [CrossRef] [PubMed]
10. Oliver, J.-A.N.; Su, Y.; Lu, X.; Kuo, P.-H.; Du, J.; Zhu, D. Bioactive glass coatings on metallic implants for biomedical applications. *Bioact. Mater.* **2019**, *4*, 261–270. [CrossRef] [PubMed]
11. Yadav, V.S.; Sankar, M.R.; Pandey, L.M. Coating of bioactive glass on magnesium alloys to improve its degradation behavior: Interfacial aspects. *J. Magnes. Alloys* **2020**, *8*, 999–1015. [CrossRef]
12. Jones, J.R. Reprint of: Review of bioactive glass: From Hench to hybrids. *Acta Biomater.* **2015**, *23*, S53–S82. [CrossRef] [PubMed]
13. Nogueira, D.M.B.; Rosso, M.P.d.O.; Buchaim, D.V.; Zangrando, M.S.R.; Buchaim, R.L. Update on the use of 45S5 bioactive glass in the treatment of bone defects in regenerative medicine. *World J. Orthop.* **2024**, *15*, 204–214. [CrossRef] [PubMed]
14. Garrido, B.; Cano, I.G.; Dosta, S. Adhesion improvement and in vitro characterisation of 45S5 bioactive glass coatings obtained by atmospheric plasma spraying. *Surf. Coat. Technol.* **2021**, *405*, 126560. [CrossRef]
15. Liu, H.; Tong, Z.; Gu, J.; Yang, D.; Liu, C.; Wang, X.; Ren, X. Effect of laser surface texturing depth and pattern on the bond strength and corrosion performance of phosphate conversion coating on magnesium alloy. *Opt. Laser Technol.* **2022**, *153*, 108164. [CrossRef]
16. Park, J.; Park, B.-I.; Son, Y.J.; Lee, S.H.; Um, S.-H.; Kim, Y.-C.; Ok, M.-R.; Sun, J.-Y.; Han, H.-S.; Jeon, H. Femtosecond laser-mediated anchoring of polymer layers on the surface of a biodegradable metal. *J. Magnes. Alloys* **2021**, *9*, 1373–1381. [CrossRef]
17. Xu, B.; Shao, Z.; Wang, Y.; Xu, R.; Zhu, C.; Lu, L.; Li, L.; Zhang, J.; Wu, X.; Zhang, C.; et al. Hierarchical coating design for AZ31 Mg alloys with corrosion resistance and bioactivity optimization. *Surf. Coat. Technol.* **2025**, *514*, 132572. [CrossRef]
18. Bajda, S.; Cholewa-Kowalska, K.; Krzyzanowski, M.; Dziadek, M.; Kopyscianski, M.; Liu, Y.; Rai, A. Laser-directed energy deposition of bioactive glass on Ti-6Al-7Nb titanium alloy substrate with highly refined grain structure. *Surf. Coat. Technol.* **2024**, *485*, 130904. [CrossRef]
19. *ASTM D3359-09*; Standard Test Methods for Measuring Adhesion by Tape Test. ASTM International: West Conshohocken, PA, USA, 2009.
20. *ISO 10993-5:2009*; Biological Evaluation of Medical Devices—Part 5: Tests for In Vitro Cytotoxicity. International Organization for Standardization: Geneva, Switzerland, 2009.

21. Zang, T.; Wang, Z.; Chen, L.; Kong, M.; Gao, S.; Ngwangwa, H.M.; Zhu, L.; Yu, W.; Zheng, H. Influence of pulse energy on surface integrity of AZ31 magnesium alloy processed by femtosecond laser shock peening. *J. Mater. Res. Technol.* **2023**, *25*, 4425–4440. [CrossRef]
22. del Val, J.; López-Cancelos, R.; Riveiro, A.; Badaoui, A.; Lusquiños, F.; Quintero, F.; Comesaña, R.; Boutinguiza, M.; Pou, J. On the fabrication of bioactive glass implants for bone regeneration by laser assisted rapid prototyping based on laser cladding. *Ceram. Int.* **2016**, *42*, 2021–2035. [CrossRef]
23. Wu, T.-C.; Joshi, S.S.; Ho, Y.-H.; Pantawane, M.V.; Sinha, S.; Dahotre, N.B. Microstructure and surface texture driven improvement in in-vitro response of laser surface processed AZ31B magnesium alloy. *J. Magnes. Alloys* **2021**, *9*, 1406–1418. [CrossRef]
24. Ouyang, S.; Wang, F.; She, J.; Qiao, L.; Fu, A.; Chen, X.; Pan, F. Recent advancements in the design of micro/nanostructured superhydrophobic surfaces on magnesium alloys. *J. Magnes. Alloys* **2025**, *13*, 457–485. [CrossRef]
25. Liu, H.; Tong, Z.; Yang, Y.; Zhou, W.; Chen, J.; Pan, X.; Ren, X. Preparation of phosphate conversion coating on laser surface textured surface to improve corrosion performance of magnesium alloy. *J. Alloys Compd.* **2021**, *865*, 158701. [CrossRef]
26. Contreras Jaimes, A.T.; de Pablos-Martín, A.; Hurle, K.; Martins de Souza e Silva, J.; Berthold, L.; Kittel, T.; Boccaccini, A.R.; Brauer, D.S. Deepening our understanding of bioactive glass crystallization using TEM and 3D nano-CT. *J. Eur. Ceram. Soc.* **2021**, *41*, 4958–4969. [CrossRef]
27. Bhaskar, P.; Kumar, R.; Maurya, Y.; Ravinder, R.; Allu, A.R.; Das, S.; Gosvami, N.N.; Youngman, R.E.; Bødker, M.S.; Mascaraque, N.; et al. Cooling rate effects on the structure of 45S5 bioglass: Insights from experiments and simulations. *J. Non-Cryst. Solids* **2020**, *534*, 119952. [CrossRef]
28. Mecca, F.G.; Bellucci, D.; Cannillo, V. Effect of Thermal Treatments and Ion Substitution on Sintering and Crystallization of Bioactive Glasses: A Review. *Materials* **2023**, *16*, 4651. [CrossRef] [PubMed]
29. Ferraris, S.; Corazzari, I.; Turci, F.; Cochis, A.; Rimondini, L.; Vernè, E. Antioxidant Activity of Silica-Based Bioactive Glasses. *ACS Biomater. Sci. Eng.* **2021**, *7*, 2309–2316. [CrossRef] [PubMed]
30. Garrido, B.; Dosta, S.; Cano, I.G. Bioactive glass coatings obtained by thermal spray: Current status and future challenges. *Bol. Soc. Esp. Ceram. V.* **2022**, *61*, 516–530. [CrossRef]
31. Rojas, O.; Prudent, M.; López, M.E.; Vargas, F.; Ageorges, H. Influence of Atmospheric Plasma Spraying Parameters on Porosity Formation in Coatings Manufactured from 45S5 Bioglass® powder. *J. Therm. Spray. Techn* **2020**, *29*, 185–198. [CrossRef]
32. Sergi, R.; Bellucci, D.; Cannillo, V. A Comprehensive Review of Bioactive Glass Coatings: State of the Art, Challenges and Future Perspectives. *Coatings* **2020**, *10*, 757. [CrossRef]
33. Ouyang, J.; Hong, X.; Gao, Y. Retardation and self-repair of erosion pits by a two-stage barrier on bioactive-glass/layered double hydroxide coating of biomedical magnesium alloys. *Surf. Coat. Technol.* **2021**, *405*, 126562. [CrossRef]
34. Bahrampour, S.; Bordbar-Khiabani, A.; Hossein Siadati, M.; Gasik, M.; Mozafari, M. Improving the inflammatory-associated corrosion behavior of magnesium alloys by Mn3O4 incorporated plasma electrolytic oxidation coatings. *Chem. Eng. J.* **2024**, *483*, 149016. [CrossRef]
35. Durán, K.S.; Hernández, N.; Rueda, L.M.; Hernández-Barrios, C.A.; Coy, A.E.; Viejo, F. Design of multilayer hybrid sol-gel coatings with bifunctional barrier-bioactive response on the Elektron 21 magnesium alloy for biomedical applications. *J. Magnes. Alloys* **2021**, *9*, 2097–2112. [CrossRef]
36. Mohan-Sathyaraj, P.; Ravichandran, K.; Sankara-Narayanan, T.S.N. Controlling the rate of degradation of Mg using magnesium fluoride and magnesium fluoride-magnesium phosphate duplex coatings. *J. Magnes. Alloys* **2022**, *10*, 295–312. [CrossRef]
37. Huang, J.; Song, G.-L.; Atrens, A.; Dargusch, M. What activates the Mg surface—A comparison of Mg dissolution mechanisms. *J. Mater. Sci. Technol.* **2020**, *57*, 204–220. [CrossRef]
38. Akshay, K.S.; Rabeeh, V.P.M.; Rahim, S.A.; Sijina, K.P.; Rajanikant, G.K.; Hanas, T. Electrophoretic deposition of alginate/bioglass composite coating on Mg Ca alloy for degradable metallic implant applications. *Surf. Coat. Technol.* **2022**, *448*, 128914. [CrossRef]
39. Maçon, A.L.B.; Kim, T.B.; Valliant, E.M.; Goetschius, K.; Brow, R.K.; Day, D.E.; Hoppe, A.; Boccaccini, A.R.; Kim, I.Y.; Ohtsuki, C.; et al. A unified in vitro evaluation for apatite-forming ability of bioactive glasses and their variants. *J. Mater. Sci. Mater. Med.* **2015**, *26*, 115. [CrossRef] [PubMed]
40. Xu, R.; Zhang, W.; Shao, Z.; Wang, Y.; Xu, B.; Zhu, C.; Wu, X.; Zhang, C.; Gao, Q.; Yu, B. Corrosion resistance and biocompatibility of magnesium alloy with bioactive glass-reinforced hydrogel composite coatings. *J. Mater. Res. Technol.* **2024**, *33*, 4176–4191. [CrossRef]
41. Nommeots-Nomm, A.; Hupa, L.; Rohanová, D.; Brauer, D.S. A review of acellular immersion tests on bioactive glasses—-influence of medium on ion release and apatite formation. *Int. J. Appl. Glass Sci.* **2020**, *11*, 537–551. [CrossRef]
42. Zine Elabidine, M.; Cherbib, M.A.; Khattech, I.; Bechrifa, A.; Schuhladen, K.; Brauer, D.S.; Boccaccini, A.R. Calorimetric approach to assess the apatite-forming capacity of bioactive glasses. *J. Non-Cryst. Solids* **2020**, *550*, 120290. [CrossRef]
43. Mehrabi, T.; Mesgar, A.S.; Mohammadi, Z. Bioactive Glasses: A Promising Therapeutic Ion Release Strategy for Enhancing Wound Healing. *ACS Biomater. Sci. Eng.* **2020**, *6*, 5399–5430. [CrossRef] [PubMed]

44. Hohenbild, F.; Arango Ospina, M.; Schmitz, S.I.; Moghaddam, A.; Boccaccini, A.R.; Westhauser, F. An In Vitro Evaluation of the Biological and Osteogenic Properties of Magnesium-Doped Bioactive Glasses for Application in Bone Tissue Engineering. *Int. J. Mol. Sci.* **2021**, *22*, 12703. [CrossRef] [PubMed]
45. Polo-Montalvo, A.; Casarrubios, L.; Serrano, M.C.; Sanvicente, A.; Feito, M.J.; Arcos, D.; Portolés, M.T. Effective Actions of Ion Release from Mesoporous Bioactive Glass and Macrophage Mediators on the Differentiation of Osteoprogenitor and Endothelial Progenitor Cells. *Pharmaceutics* **2021**, *13*, 1152. [CrossRef] [PubMed]
46. Kim, J.; Gilbert, J.L.; Lv, W.W.; Du, P.; Pan, H. Reduction reactions dominate the interactions between Mg alloys and cells: Understanding the mechanisms. *Bioact. Mater.* **2025**, *45*, 363–387. [CrossRef] [PubMed]
47. Thamma, U.; Kowal, T.J.; Falk, M.M.; Jain, H. Nanostructure of bioactive glass affects bone cell attachment via protein restructuring upon adsorption. *Sci. Rep.* **2021**, *11*, 5763. [CrossRef] [PubMed]

Disclaimer/Publisher's Note: The statements, opinions and data contained in all publications are solely those of the individual author(s) and contributor(s) and not of MDPI and/or the editor(s). MDPI and/or the editor(s) disclaim responsibility for any injury to people or property resulting from any ideas, methods, instructions or products referred to in the content.